

ARTICLE TYPE

Bayesian Calibration for Large-Scale Fluid Structure Interaction Problems Under Embedded/Immersed Boundary Framework

Shunxiang Cao¹ | Daniel Zhengyu Huang*²

¹Department of Mechanical and Civil Engineering, California Institute of Technology, CA, USA

²Department of Environmental Science and Engineering, Department of Computing Mathematical Sciences, California Institute of Technology, CA, USA

Correspondence

*Daniel Zhengyu Huang, Department of Environmental Science and Engineering, Department of Computing Mathematical Sciences, California Institute of Technology. Email: dzhuang@caltech.edu

Abstract

Bayesian calibration is widely used for inverse analysis and uncertainty analysis for complex systems in the presence of both computer models and observation data. In the present work, we focus on large-scale fluid-structure interaction systems characterized by large structural deformations. Numerical methods to solve these problems, including embedded/immersed boundary methods, are typically not differentiable and lack smoothness. We propose a framework that is built on unscented Kalman filter/inversion to efficiently calibrate and provide uncertainty estimations of such complicated models with noisy observation data. The approach is derivative-free and non-intrusive, and is of particular value for the forward model that is computationally expensive and provided as a black box which is impractical to differentiate. The framework is demonstrated and validated by successfully calibrating the model parameters of a piston problem and identifying the damage field of an airfoil under transonic buffeting.

KEYWORDS:

Fluid-structure interaction; Derivative-free optimization; Bayesian calibration; Embedded/Immersed boundary method; Uncertainty quantification

1 | INTRODUCTION

Fluid-Structure Interaction (FSI) problems arise in many scientific and engineering applications including, to name only a few, aircraft aeroelasticity^{1,2,3}, parachute inflation dynamics^{4,5,6}, hemodynamics^{7,8,9}, and lithotripsy^{10,11}. Besides the development of mathematical models, seamless integration of observation data with these models starts to play a significant role to improve the prediction and quantify uncertainty for FSI, for example, calibration of hemodynamic model parameters to match patient data^{12,13,9} and structural damage detection using sensor data and a digital twin^{14,15,16}. The integration can be formulated as a data-based calibration problem. And major associated challenges include:

- Observation data are noisy;
- The calibration problems might not be done for the single fluid or structure subsystem without FSI coupling, due to strong fluid-structure coupling and complex mechanism (e.g., viscoelasticity⁹), which requires FSI solvers with advanced numerical methods particularly designed for the applications of interest;

⁰**Abbreviations:** FSI, fluid structure interaction; EBM, embedded boundary method; UKI, unscented Kalman inversion; CFD, computational fluid dynamics; AMR, adaptive mesh refinement; MCMC Markov chain Monte Carlo; ETKI, ensemble transform Kalman inversion.

- The FSI solvers might be given as a black box (difficult to calculate the derivative in practice), or the solvers are not differentiable due to the numerical methods (e.g., embedded boundary method and adaptive mesh refinement) or the physical nature (fracture);
- Each forward FSI evaluation is expensive for real-world applications.

Therefore, an efficient non-intrusive algorithm for calibration and uncertainty quantification is highly desirable.

The present work focuses on data-based calibration for FSI problems where the structure undergoes large displacements, large rotations and/or deformations, as well as topological changes. A popular class of methods for solving this kind of FSI problems are the Embedded^{17,18,19,20,21} or Immersed Boundary Methods^{22,23,24,25,26,27,28} (EBMs or IBMs). These methods compute fluid flow on non-body-fitted computational fluid dynamics (CFD) meshes in which discrete representations of wet surfaces of obstacles are embedded or immersed. There are variants under other names, including cut cell methods^{29,30,31}, fictitious domain methods^{32,33,34,35,36}, ghost fluid-structure methods³⁷, and immersed boundary–Lattice Boltzmann methods^{38,39}. However, as for data-based calibration, EBMs and IBMs might not be favorable, because they are generally not differentiable and the quantities of interest, like surface stresses and forces, require special treatments to retain smoothness^{25,40,41,42,43}. The non-differentiation and lack of smoothness are rooted in the enforcement of fluid-structure interface conditions on a non-interface-conforming mesh. More specifically, the stencils, which are used to evaluate discrete delta function or reconstruct fluid states at the "sharp interface", keep changing along with the moving interface. And the status of a node may switch between real fluid node and ghost fluid node as the structure moves through the fixed mesh, producing severe oscillations in the solution. These discrete events render adjoint-based optimization approaches almost impractical for the calibration. Moreover, EBMs and IBMs are generally combined with adaptive mesh refinement (AMR)^{44,45,46} for better resolution of the fluid-structure interface. AMR "discretely" adds and removes fluid nodes for refinement and coarsening, which further complicates the differentiation. Therefore, in the present work, we focus on derivative-free approaches for calibration. It is worth mentioning although the calibration approach is demonstrated with the EBM, it is equally applicable to its body-fitted counterpart—arbitrary Lagrangian-Eulerian (ALE) approach^{47,48,49,50,51,52,53}, which relies on mesh motion, deformation schemes, and local remeshing^{54,48,55} to maintain mesh conformity at the fluid-structure interface.

Derivative-free Bayesian calibration or inversion^{56,57} generally starts with the observation error model,

$$y = \mathcal{G}(\theta) + \eta, \quad (1)$$

where the forward operator $\mathcal{G} : \mathbb{R}^{N_\theta} \rightarrow \mathbb{R}^{N_y}$ maps the unknown model parameter vector $\theta \in \mathbb{R}^{N_\theta}$ to the observation vector $y \in \mathbb{R}^{N_y}$. Specifically, the operator \mathcal{G} represents the FSI solver with proper initial and boundary conditions. For a given observation, the observational noise η is unknown, but it is assumed to statistically follow a known distribution. To be concrete we will assume that it is drawn from a Gaussian with distribution $\mathcal{N}(0, \Sigma_\eta)$. Given a guess of the distribution of θ , represented by a prior density function $p_0(\theta)$, Bayesian calibration aims to estimate the posterior distribution of θ that satisfies

$$p(\theta) \propto \exp(-\Phi(\theta))p_0(\theta) \quad \text{with} \quad \Phi(\theta) = \frac{1}{2} \|\Sigma_\eta^{-\frac{1}{2}}(y - \mathcal{G}(\theta))\|^2, \quad (2)$$

where $\Phi(\theta)$ denotes the misfit between the modeled and observed data. The resulting $p(\theta)$ is supposed to provide a good confidence interval of the truth parameter. In the present work, we assume there are enough observation data, and use improper uniform prior $p_0 \propto 1$ to let the data speak for itself. It is worth noticing that the maximum a posteriori (MAP) estimation for θ with the improper uniform prior corresponds to the minimizer of $\Phi(\theta)$. Mostly, the calibration is simplified and reformulated as a nonlinear least-square optimization problem to find optimal θ that satisfies

$$\theta = \arg \min_{\theta} \frac{1}{2} \|\Sigma_\eta^{-\frac{1}{2}}(y - \mathcal{G}(\theta))\|^2 \quad (3)$$

instead of its distribution. In this case, the major challenge of the optimization also lies in the aforementioned fact that \mathcal{G} is not differentiable.

Traditional methods for derivative-free Bayesian calibration to estimate the posterior distribution, such as Markov chain Monte Carlo^{58,59,60} (MCMC), typically require many iterations—often more than 10^4 —to reach statistical convergence. Given that each forward run can be expensive, conducting so many runs is computationally unaffordable, rendering MCMC impractical for real-world FSI calibrations.

In the present work, we employ the Kalman inversion for the Bayesian calibration, which approximates the posterior distribution as Gaussian distribution and generally requires $O(10)$ iterations. Kalman inversion derived from Kalman filter⁶¹ and its variants, including but not limited to extended Kalman filter⁶², ensemble Kalman filter⁶³, unscented Kalman filter^{64,65}, and

cubature Kalman filter⁶⁶, which are developed to sequentially update the probability distribution of states in partially observed dynamics. Kalman filtering is a two-step procedure: (1) the prediction step, where the state is computed forward in time; (2) the analysis step, where the state and its uncertainty are corrected to take into account the observation data. In the analysis step, Kalman filters use Gaussian ansatz to formulate Kalman gain to assimilate the observation and update the distribution. Numerous applications of Kalman filters, including weather forecasts^{63,67,68} and guidance, navigation, and control of vehicles^{62,64,66} demonstrate empirically that Kalman filters can not only calibrate the model prediction, but also provides uncertainty information for state estimation problems. Kalman inversion which applies Kalman filters for parameter calibration originates from^{69,65,70,71,72,73,74}. Specifically, the parameter-to-data map (Eq. (1)) is first paired with a stationary stochastic dynamical system for the parameter, and then techniques from Kalman filtering are iteratively applied to estimate the parameter given the observation data. Consider the following stochastic dynamical system⁷⁴,

$$\text{evolution:} \quad \theta_{n+1} = \theta_n + \omega_{n+1}, \quad \omega_{n+1} \sim \mathcal{N}(0, \Sigma_\omega) \quad (4a)$$

$$\text{observation:} \quad y_{n+1} = \mathcal{G}(\theta_{n+1}) + v_{n+1}, \quad v_{n+1} \sim \mathcal{N}(0, \Sigma_v) \quad (4b)$$

where θ_{n+1} is the unknown parameter vector at the artificial time $n + 1$, and $y_{n+1} = y$ is the observation, the artificial evolution error ω_{n+1} and artificial observation error v_{n+1} are mutually independent, zero-mean Gaussian sequences with covariances Σ_ω and Σ_v , respectively. It is worth distinguishing the artificial time from the real time for time-dependent problems. In the present work, each artificial time step represents a Kalman filtering iteration in which the observation y may consist of the time-series observation data from a full forward simulation. Given its non-intrusive nature, Kalman inversion has been widely used as an optimization method for parameter estimation^{75,76,77,78,79,80,81,82}, especially for problems where the forward model is expensive and provided as a black box that is impractical to differentiate.

Specifically, unscented Kalman inversion^{65,74} (UKI) is employed in the present work, where unscented Kalman filter^{64,83,65} is iteratively applied to the stationary stochastic dynamics (Eq. (4)). From the Bayesian point of view, UKI approximates the parameter distribution by a Gaussian and allows to well approximate the mean and covariance of the posterior distribution. Theoretical guarantees for both linear and nonlinear well-posed inverse problems are presented in⁸⁴. From the optimization point of view, UKI converges exponentially fast for linear calibration problems⁷⁴; UKI performs like a generalized Levenberg-Marquardt Algorithm with a smoothed data-misfit for nonlinear calibration problems⁷⁴. It has been demonstrated effective for handling noisy observation data and solving even chaotic problems^{74,85,84}. The Tikhonov regularization strategies to overcome ill-posedness and speed-up strategies, including the low-rank approximation of the covariance and low-resolution reduced-order models, are thoroughly studied in the works of Huang *et al.*^{74,85}.

The remainder of this paper is organized as follows. In Section 2, Bayesian calibration and unscented Kalman inversion are introduced. Section 3 provides an overview of the FSI under embedded boundary framework. Numerical examples that demonstrate and validate the proposed approach are presented in Section 4, involving a 1D piston problem and a challenging 3D airfoil damage detection problem with transonic buffeting flows. Finally, conclusions are offered in Section 5.

2 | BAYESIAN CALIBRATION

Recall that the Bayesian calibration approach starts to pair the parameter-to-data relationship encoded in Eq. (1) with the stochastic dynamical system for the parameter (Eq. (4)). A useful way to think of the procedure is through the analogy to pseudo-time stepping for solving steady-state problem. To approximate the posterior distribution, we employ techniques from unscented Kalman filtering to iteratively update the conditional probability density function p_n of $\theta_n | Y_n$, where $Y_n := \{y_1, y_2, \dots, y_n\}$ is the observation set at artificial time n , until its convergence. The probability density function p_n is approximated to be Gaussian¹ $\mathcal{N}(m_n, C_n)$ with mean m_n and covariance C_n for the sake of efficiency. Hence, in Subsection 2.1 we first introduce a Gaussian approximation algorithm, which maps the space of Gaussian measures into itself at each step of the iteration; Subsection 2.2 shows how this algorithm can be made practical by applying a quadrature rule (i.e., unscented transform) to evaluate certain integrals appearing in the conceptual Gaussian approximation, which leads to the UKI algorithm. In Subsection 2.3, the UKI is compared with other optimization approaches.

¹A justification of using Gaussian to approximate the posterior distribution (2) is from the Bernstein-von Mises theorem^{86,87,88,89}, which states the posterior distribution becomes asymptotically a multivariate normal distribution with the increasing of data under certain regularity conditions.

2.1 | Gaussian Approximation Algorithm

At each iteration n , p_n is updated through the prediction and analysis steps^{90,91}: $p_n \mapsto \hat{p}_{n+1}$, and then $\hat{p}_{n+1} \mapsto p_{n+1}$, where \hat{p}_{n+1} denotes the conditional probability density function of $\theta_{n+1}|Y_n$.

In the prediction step, $\hat{p}_{n+1} = \mathcal{N}(\hat{m}_{n+1}, \hat{C}_{n+1})$ is also Gaussian under Eq. (4a) and satisfies

$$\hat{m}_{n+1} = \mathbb{E}[\theta_{n+1}|Y_n] = m_n, \quad \hat{C}_{n+1} = \text{Cov}[\theta_{n+1}|Y_n] = C_n + \Sigma_\omega. \quad (5)$$

In the analysis step, the joint distribution of $\{\theta_{n+1}, y_{n+1}\}|Y_n$ can be approximated by a Gaussian distribution

$$\mathcal{N}\left(\begin{bmatrix} \hat{m}_{n+1} \\ \hat{y}_{n+1} \end{bmatrix}, \begin{bmatrix} \hat{C}_{n+1} & \hat{C}_{n+1}^{\theta p} \\ \hat{C}_{n+1}^{\theta p T} & \hat{C}_{n+1}^{pp} \end{bmatrix}\right), \quad (6)$$

with

$$\begin{aligned} \hat{y}_{n+1} &= \mathbb{E}[\mathcal{G}(\theta_{n+1})|Y_n], \\ \hat{C}_{n+1}^{\theta p} &= \text{Cov}[\theta_{n+1}, \mathcal{G}(\theta_{n+1})|Y_n], \\ \hat{C}_{n+1}^{pp} &= \text{Cov}[\mathcal{G}(\theta_{n+1})|Y_n] + \Sigma_v. \end{aligned} \quad (7)$$

Conditioning the Gaussian in (6) to find $\theta_{n+1}|\{Y_n, y_{n+1}\} = \theta_{n+1}|Y_{n+1}$ gives the following expressions for the mean m_{n+1} and covariance C_{n+1} of the approximation to p_{n+1} :

$$\begin{aligned} m_{n+1} &= \hat{m}_{n+1} + \hat{C}_{n+1}^{\theta p} (\hat{C}_{n+1}^{pp})^{-1} (y_{n+1} - \hat{y}_{n+1}), \\ C_{n+1} &= \hat{C}_{n+1} - \hat{C}_{n+1}^{\theta p} (\hat{C}_{n+1}^{pp})^{-1} \hat{C}_{n+1}^{\theta p T}. \end{aligned} \quad (8)$$

Equations (5) to (8) establish a conceptual algorithm for application of Gaussian approximation for Bayesian calibration. And the integrals appearing in Eq. (7) are approximated by the unscented approach, which is detailed in the following subsection.

2.2 | Unscented Kalman Inversion

The unscented Kalman inversion uses the following unscented transform⁷⁴ to evaluate Eq. (7):

Definition 1. Let denote Gaussian random variable $\theta \sim \mathcal{N}(m, C) \in \mathbb{R}^{N_\theta}$, $2N_\theta + 1$ symmetric sigma points are chosen deterministically:

$$\theta^0 = m \quad \theta^j = m + c_j[\sqrt{C}]_j \quad \theta^{j+N_\theta} = m - c_j[\sqrt{C}]_j \quad (1 \leq j \leq N_\theta), \quad (9)$$

where $[\sqrt{C}]_j$ is the j th column of the Cholesky factor of C . The quadrature rule approximates the mean and covariance of the transformed variable $\mathcal{G}_i(\theta)$ as follows,

$$\mathbb{E}[\mathcal{G}_i(\theta)] \approx \mathcal{G}_i(\theta^0) \quad \text{Cov}[\mathcal{G}_1(\theta), \mathcal{G}_2(\theta)] \approx \sum_{j=1}^{2N_\theta} W_j^c (\mathcal{G}_1(\theta^j) - \mathbb{E}\mathcal{G}_1(\theta))(\mathcal{G}_2(\theta^j) - \mathbb{E}\mathcal{G}_2(\theta))^T. \quad (10)$$

Here these constant weights are

$$\begin{aligned} c_j &= \sqrt{N_\theta + \lambda} \quad (j = 1, \dots, N_\theta) & W_j^c &= \frac{1}{2(N_\theta + \lambda)} \quad (j = 1, \dots, 2N_\theta), \\ \lambda &= a^2(N_\theta + \kappa) - N_\theta & \kappa &= 0 & a &= \min\left\{\sqrt{\frac{4}{N_\theta + \kappa}}, 1\right\}. \end{aligned}$$

The aforementioned unscented transform is different from the original unscented transform⁹². The modification we employ here replaces the original 2nd-order approximation of the $\mathbb{E}[\mathcal{G}_i(\theta)]$ with its 1st-order counterpart, in order to avoid negative weights.

When the unscented transform is applied to make such approximation, we obtain the unscented Kalman inversion algorithm. Following the work of Huang *et al.*⁸⁴, the hyperparameters are chosen as

$$\Sigma_v = 2\Sigma_\eta \quad \text{and} \quad \Sigma_\omega = C_n, \quad (11)$$

at the n -th iteration. This guarantees that the converged mean and covariance well approximate those of the posterior distribution (Eq. (2)) with an uninformative prior for identifiable inverse problems ($N_y \gg N_\theta$) under certain regularization conditions. The algorithm for unscented Kalman inversion is summarized in Algorithm 1.

Algorithm 1 Unscented Kalman Inversion

- 1: **function** UKI(\mathcal{G} , m_0 , C_0 , y , Σ_η)
- 2: **while** $n \leq N_{\max}$ or non-converge **do**
- 3: Prediction step :

$$\hat{m}_{n+1} = m_n \quad \hat{C}_{n+1} = 2C_n$$

- 4: Generate sigma points :

$$\begin{aligned} \hat{\theta}_{n+1}^0 &= \hat{m}_{n+1} \\ \hat{\theta}_{n+1}^j &= \hat{m}_{n+1} + c_j [\sqrt{\hat{C}_{n+1}}]_j \quad (1 \leq j \leq N_\theta) \\ \hat{\theta}_{n+1}^{j+N_\theta} &= \hat{m}_{n+1} - c_j [\sqrt{\hat{C}_{n+1}}]_j \quad (1 \leq j \leq N_\theta) \end{aligned}$$

- 5: Analysis step :

$$\begin{aligned} \hat{y}_{n+1}^j &= \mathcal{G}(\hat{\theta}_{n+1}^j) \quad (0 \leq j \leq 2N_\theta) \\ \hat{y}_{n+1} &= \hat{y}_{n+1}^0 \\ \hat{C}_{n+1}^{\theta p} &= \sum_{j=1}^{2N_\theta} W_j^c (\hat{\theta}_{n+1}^j - \hat{m}_{n+1})(\hat{y}_{n+1}^j - \hat{y}_{n+1})^T \\ \hat{C}_{n+1}^{pp} &= \sum_{j=1}^{2N_\theta} W_j^c (\hat{y}_{n+1}^j - \hat{y}_{n+1})(\hat{y}_{n+1}^j - \hat{y}_{n+1})^T + 2\Sigma_\eta \\ m_{n+1} &= \hat{m}_{n+1} + \hat{C}_{n+1}^{\theta p} (\hat{C}_{n+1}^{pp})^{-1} (y - \hat{y}_{n+1}) \\ C_{n+1} &= \hat{C}_{n+1} - \hat{C}_{n+1}^{\theta p} (\hat{C}_{n+1}^{pp})^{-1} \hat{C}_{n+1}^{\theta p T} \end{aligned} \tag{12}$$

- 6: **end while**
 - 7: **return** m_{n+1} , C_{n+1}
 - 8: **end function**
-

2.3 | Nonconvex Optimization: A Comparative Study

Due to the "discrete" events existing in the EBMs and IBMs, the objective function (likelihood function) $\Phi(\theta)$ might be lacking of smoothness and might have multiple local optima, which hinders classical optimization approaches. However, we find UKI, as an ensemble-based method, has a better performance in avoiding local optima.

In this section, UKI is compared with three other optimization methods, including derivative free ensemble transformed Kalman inversion (ETKI) described in the Appendix B.2 of the work of Huang *et al.*⁸⁵ and gradient-based Newton and BFGS (Broydon-Fletcher-Goldfarb-Shanno) methods, for a nonconvex one-dimensional nonlinear least square problem (3) with

$$\mathcal{G}(\theta) = \sin(5\theta) + \theta \quad y = 0 \quad \Sigma_\eta = [1.0].$$

This problem has 5 global minimizers: $\theta = -0.981, -0.821, 0, 0.821, 0.981$, and numerous local minimizers. The landscape of the objective function is depicted in Fig. 1. Three different initial guesses are chosen: $m_0 = 10, m_0 = 11$, and $m_0 = 12$, and for UKI and ETKI the initial covariance is $C_0 = \mathbb{I}$. The ensemble size of the ETKI is $J = 10$, which is larger than the number of σ -points used in UKI. For Newton and BFGS methods, we use library Optim.jl⁹³ with the line search method proposed in the work of Hager & Zhang⁹⁴.

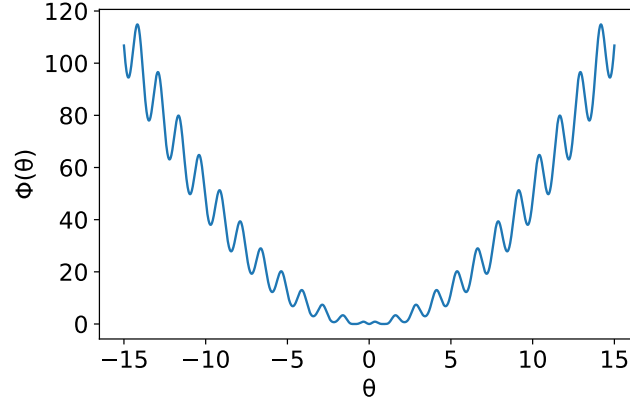


FIGURE 1 The landscape of the objective function for the illustrative one-dimensional problem.

The convergence histories obtained with these approaches are depicted in Fig. 2. Both Newton and BFGS methods are prone to be trapped in local optima, primarily because only local gradient and Hessian information are used in the solution process. However, neither ETKI nor UKI are trapped in local optima. For UKI, although there is no guarantee that the global minimizer can be found, the ensemble $\{\theta_{n+1}^j\}$ around the mean value \hat{m}_{n+1} brings non-local information and has averaging effect⁷⁴ on the landscape. And therefore, it is able to avoid local optima. Compared to UKI, ETKI suffers from random noise, and the estimated means oscillate around the optima.

3 | FLUID STRUCTURE INTERACTION UNDER EMBEDDED BOUNDARY FRAMEWORK

3.1 | Governing Equations

We consider solving fluid-structure interaction problems involving large structural deformations and even structural damage. Let Ω_F and Ω_S denote the fluid and the structural subdomains. The fluid is assumed to be compressible and inviscid, governed by the following Euler equations in the Eulerian frame

$$\frac{\partial W(x, t)}{\partial t} + \nabla \cdot \mathcal{F}(W) = 0, \quad \forall x \in \Omega_F(t), t > 0, \quad (13)$$

$$W = \begin{bmatrix} \rho \\ \rho v \\ \rho e_t \end{bmatrix}, \quad \mathcal{F} = \begin{bmatrix} \rho v^T \\ \rho v \otimes v + p \mathbb{I} \\ (\rho e_t + p) v^T \end{bmatrix},$$

where ρ , v , p and e_t denote the fluid density, velocity, pressure, and the total energy per unit mass, respectively. \mathbb{I} denotes an identity matrix. The fluid is assumed to be a perfect gas, and the following equation of state is applied to close Eq. (13)

$$p = (\gamma_G - 1) \rho e, \quad (14)$$

where the heat capacity ratio γ_G is set to be 1.4 in this work, and e denotes the internal energy per unit mass.

The dynamics of structure is governed by the following equation of motion in the Lagrangian frame

$$\rho_s \ddot{u}(X, t) - \nabla \cdot \sigma = b, \quad \forall X \in \Omega_S(0), t > 0, \quad (15)$$

where u denotes displacement, ρ_s the material's mass density and σ the Cauchy or Piola-Kirchhoff stress tensor. b denotes the body force acting in Ω_S , which is assumed to be zero in this study. The dot above a variable represents partial derivative with respect to time. Given a structural material of interest, the closure of (15) is performed by specifying a constitutive law that relates the stress tensor σ to the strain tensor e .

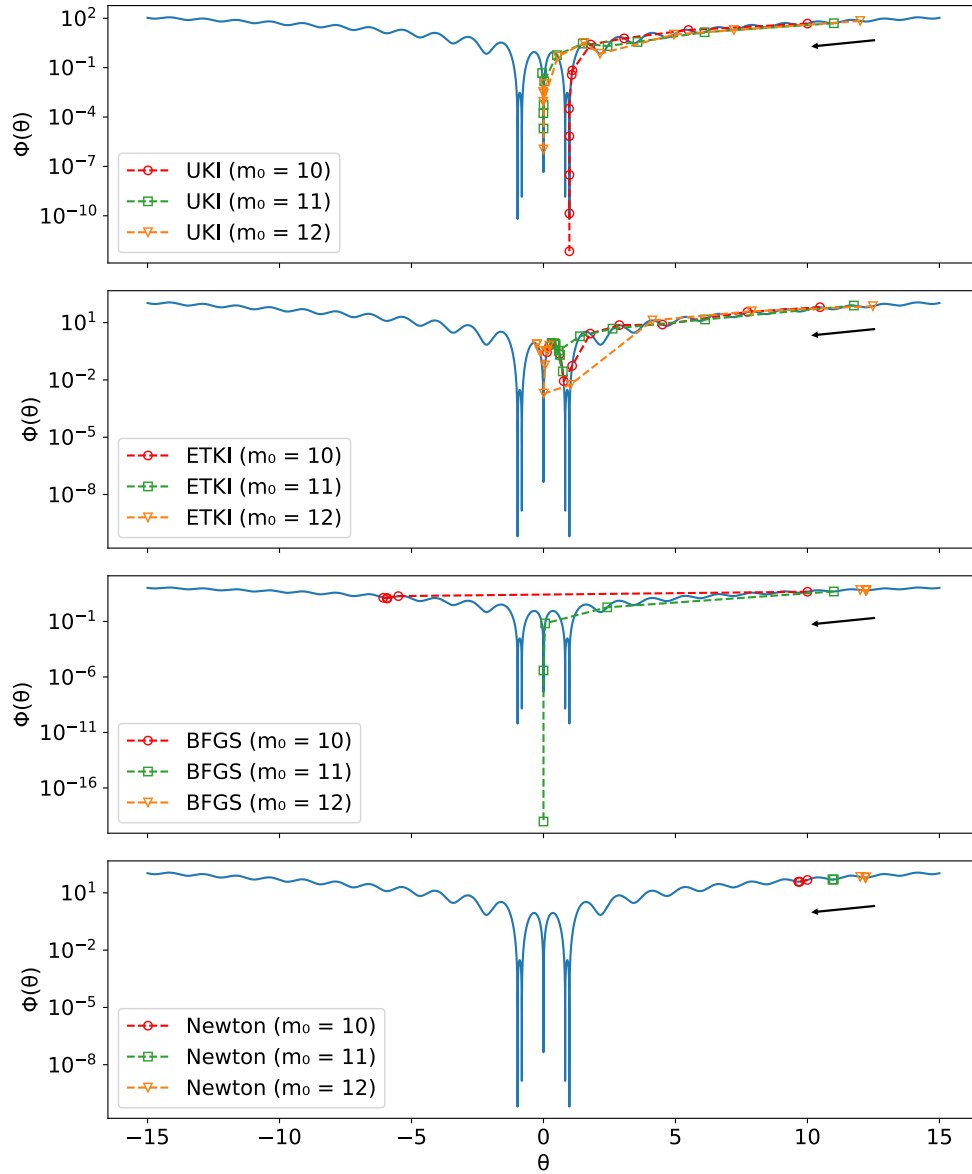


FIGURE 2 Convergence histories of different optimization approaches initialized at $m_0 = 10$ (red circle dashed lines), $m_0 = 11$ (green square dashed lines), and $m_0 = 12$ (orange triangle dashed lines) for the illustrative one-dimensional problem.

The fluid-structure interface, $\Gamma_{FS} = \partial\Omega_F(t) \cap \partial\Omega_S(t)$, is assumed to be impermeable, at which we enforce the continuity of normal velocity and surface traction, i.e.,

$$\begin{aligned} (v - \dot{u}) \cdot n &= 0, & \text{on } \Gamma_{FS}, \\ -pn &= \sigma \cdot n, & \text{on } \Gamma_{FS}, \end{aligned} \quad (16)$$

where n denotes the unit normal to Γ_{FS} .

3.2 | An Embedded Boundary Computational Framework

The above coupled problem is solved by a recently developed fluid-structure coupled computational framework^{95,18,96,21,97}. The framework couples a finite volume CFD solver with a finite element computational structural dynamics solver using an embedded boundary method and a partitioned coupling procedure. The framework has been verified and validated on various

applications, including dynamic implosion of underwater cylindrical shells^{18,96,98}, F/A-18 vertical tail buffeting²⁰, and Mars landing parachute inflation dynamics^{99,5,100}.

3.2.1 | FIVER: A Finite Volume Method Based on Exact Riemann Solver

The fluid governing equation is semi-discretized in an augmented fluid domain $\tilde{\Omega} = \Omega_F \cup \Omega_S$, using an unstructured, node centered, non-interface-conforming finite volume mesh, denoted by $\tilde{\Omega}^h$. Figure 3 presents an example to illustrate the non-interface-conforming mesh. Within each control volume (C_i) in $\tilde{\Omega}^h$, Eq. (13) is integrated as

$$\frac{\partial W_i}{\partial t} + \frac{1}{\|C_i\|} \sum_{j \in Nei(i)} \int_{\partial C_{ij}} \mathcal{F}(W) \cdot n_{ij} dS = 0, \quad (17)$$

where W_i denotes the average of W in C_i , $\|C_i\|$ denotes the volume of C_i , $Nei(i)$ denotes the set of nodes connected to node i by an edge, $\partial C_{ij} = \partial C_i \cap \partial C_j$, and n_{ij} is the unit normal to ∂C_{ij} . Away from the fluid-structure interface, the flux through each segment ∂C_{ij} in Eq. (17) is approximated using Roe's (or any other similar) approximate Riemann solver¹⁰¹ equipped with a MUSCL technique¹⁰² and a slope limiter.

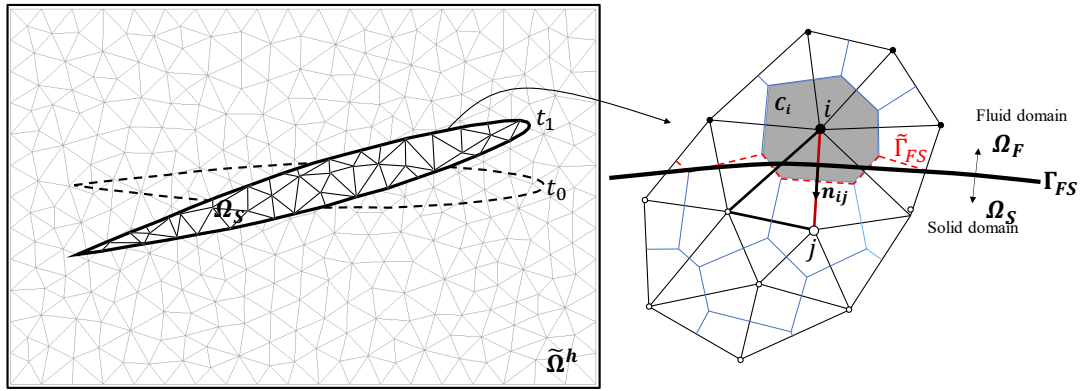


FIGURE 3 Illustration of the non-interface-conforming mesh under embedded boundary framework.

At the embedded fluid-structure interface, the flux in Eq. (17) is approximated with the reconstructed fluid state vector, which satisfies the transmission conditions (16). The reconstruction is through solving a one-dimensional fluid-solid Riemann problem. Specifically, as shown in the right figure in Figure 3, suppose node i belongs to the fluid subdomain, node j belongs to the solid subdomain, and edge i - j intersects the embedded interface Γ_{FS} . We construct the following one-dimensional fluid-solid Riemann problem along n_S , the unit normal of Γ_{FS} (toward the structure) at its intersection with edge i - j , at each time-instance t_n

$$\frac{\partial w}{\partial \tau} + \frac{\partial \mathcal{F}(w)}{\partial \xi} = 0, \quad 0 \leq \tau \leq \Delta t^n, \quad \xi < (\dot{u}_0 \cdot n_S)\tau, \quad (18)$$

$$w(\xi, 0) = w_i, \quad \xi < 0, \quad (19)$$

$$v((\dot{u}_0 \cdot n_S)\tau, \tau) = \dot{u}_0 \cdot n_S, \quad 0 \leq \tau \leq \Delta t_n, \quad (20)$$

ξ is the spatial coordinate along the one-dimensional axis aligned with n_S and centered at the intersection point. The initial state w_i is the projection of W_i on n_S , i.e.

$$w_i = \begin{bmatrix} \rho_i \\ \rho_i(v_i \cdot n_S) \\ \rho_i(e_i + \frac{1}{2}(v_i \cdot n_S)^2) \end{bmatrix}. \quad (21)$$

\dot{u}_0 denotes the velocity of the structure at t_n . The exact solution of this Riemann problem can be derived analytically. And the state variables and the tangential fluid velocity are used to reconstruct the fluid state vector at the fluid-structure interface. The

resulting semi-discretization of Eq. (13) can be written in a compact form as

$$\frac{d\mathbf{W}^h}{dt} + \mathbf{V}^{-1}\mathbf{F}(\mathbf{W}^h) = 0, \quad (22)$$

where \mathbf{W}^h , \mathbf{V} , and $\mathbf{F}(\mathbf{W}^h)$ denote the vector of semidiscrete fluid state variable, the diagonal matrix storing the volume of control volumes, and the vector of numerical flux, respectively.

3.2.2 | A Finite Element Structural Solver

The structural governing equation is solved using a standard Galerkin finite element method. The semi-discretized equation is written as

$$\mathbf{M}\frac{\partial^2\mathbf{u}^h}{\partial t^2} + \mathbf{f}^{int}\left(\mathbf{u}^h, \frac{\partial\mathbf{u}^h}{\partial t}\right) = \mathbf{f}^{ext}, \quad (23)$$

where \mathbf{M} denotes the mass matrix, \mathbf{u}^h denotes the discrete displacement vector. \mathbf{f}^{int} and \mathbf{f}^{ext} denote the discrete internal force and external force vector, respectively. Based on the dynamics interface condition (Eq. (16)), the fluid-induced external forces are computed by integrating the fluid pressure over the embedded interface. Additional details can be found in Section 3.8.3 in the work of Main¹⁰³.

3.2.3 | Partitioned Coupling Procedure

We employ a partitioned procedure to advance the fluid subsystem (22) and structure subsystem (23) in time, following the work of Farhat *et al.*⁹⁵. Specifically, the fluid and structural discretized equations are solved independently with different time integrators. The two solvers exchange information at the fluid-structure interface once per time step in a staggered manner, i.e., the fluid and solid time steps are offset by half a step. This is a designed feature to achieve second-order accuracy in time while maintaining optimal numerical stability.

4 | NUMERICAL RESULTS

In this section, we apply the unscented Kalman inversion and the embedded boundary framework presented in Sections 2 and 3 to calibrate parameters, as well as quantify their uncertainty, for two FSI problems with noisy observation data. The first case is a one-dimensional piston model problem, where the damping coefficient, the spring stiffness, and the initial fluid pressure are calibrated from the piston displacement. The second case is a challenging three-dimensional aeroelasticity problem of a damaged airfoil, where the damage field, specifically the coefficients of first 5 modes, is inferred from the displacement during its transonic buffet. For both cases, we prescribe a reference value for the parameters of interest and generate the time-series observation data in which additional Gaussian random noise is added. Then, using the noisy data, we solve the Bayesian calibration problem to retrieve the predefined parameters and associated uncertainties. The code associated with these two test cases is accessible online: <https://github.com/Zhengyu-Huang/InverseProblems.jl>.

4.1 | Piston Problem

We first consider a canonical FSI model problem: a one-dimensional piston problem depicted in Fig. 4. The inviscid fluid is governed by the one-dimensional Euler equations defined within domain $x \in [0, 1 - u]$, where u is the displacement of the piston. The fluid is initially at rest, with initial density, velocity, and pressure given by:

$$\rho_0 = 1.225, \quad v_0 = 0, \quad p_0 = 2.0.$$

No-penetration wall boundary condition is imposed on the left end of the fluid domain. On the right, the fluid interacts with a piston. The piston is connected with a spring and a damper that are attached to a wall on the right at $x = 1$. The dynamics of the piston can be described by the second order ordinary differential equation:

$$m_s\ddot{u} + c_s\dot{u} + k_s u = f^{ext},$$

where the mass coefficient is $m_s = 1$, the damping coefficient is $c_s = 0.5$, and the spring stiffness is $k_s = 2$. The external force f_{ext} is the fluid pressure load on the piston:

$$f^{ext}(t) = p(x_p(t)),$$

where $x_p(t) = 1 - u(t)$. The piston is initialized at $x = 1$, with $u(0) = 0$ and $\dot{u}(0) = 0$.

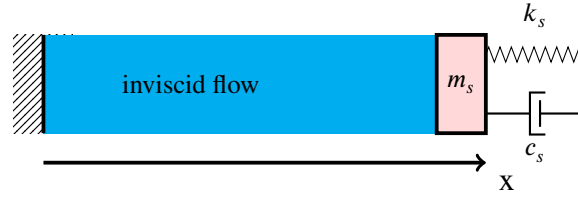


FIGURE 4 One-dimensional piston system

For the forward problem, the computational domain is semi-discretized by a uniform grid with $\Delta x = 5 \times 10^{-3}$. The explicit 2nd-order Runge-Kutta time integrator is used for the fluid and implicit 2nd-order mid-point rule time integrator is applied for the structure with a constant time step $\Delta t = 10^{-3}$. The coupled system is integrated till the final time $T = 1$.

For the inverse problem, we consider two scenarios:

1. calibrate only the structure parameters $\theta = [c_s; k_s]$ with $N_\theta = 2$;
2. calibrate both structure parameters and fluid initial pressure $\theta = [c_s; k_s; p_0]$ with $N_\theta = 3$.

The observation data consist of $N_y = 100$ piston displacement measurements collected at every 10^{-2} till $T = 1$. These observation data are generated with reference parameters and corrupted with zero-mean random Gaussian noise with standard deviation $\sigma_\eta = 2 \times 10^{-3}$. The observation data are depicted in Fig. 5-left; and the corresponding fluid states at the end time is depicted in Fig. 5-right, the rarefaction wave is generated in the flow due to the receding motion of the piston.

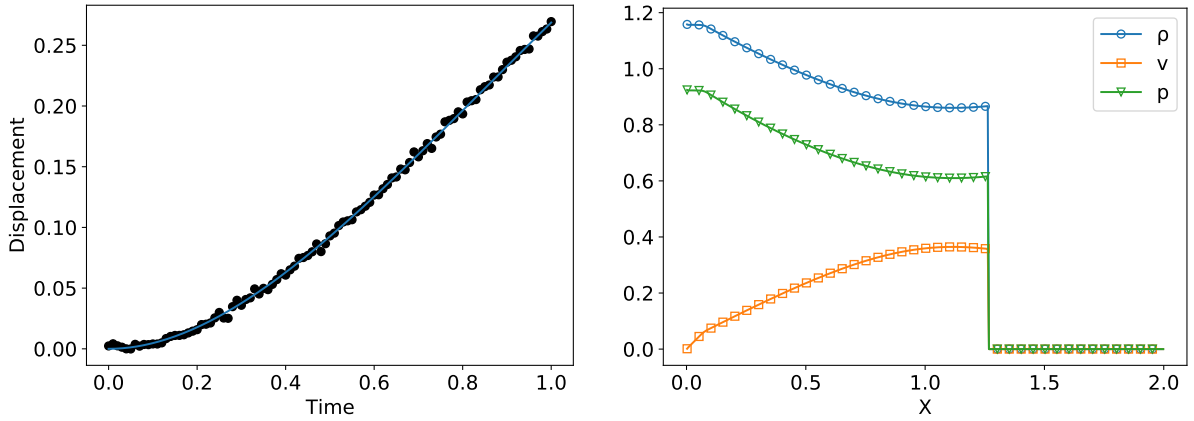


FIGURE 5 Left: the displacement of the piston with 100 noisy measurements (black dots); Right: the fluid states at the end time.

For both scenarios, the UKI is initialized with $\theta_0 \sim \mathcal{N}(1, 0.1^2 \mathbf{I})$. The estimated parameters and associated $2\text{-}\sigma$ confidence intervals for each component at each iteration are depicted in Fig. 6. The UKI converges efficiently. Reference values falls within the confidence interval with high probability, although the uncertainty is larger for the 3-parameter scenario. The reference posterior distribution is approximated by the random walk MCMC method with a step size 1.0×10^{-2} and 5×10^4 samples (with a 10^4 sample burn-in period). The posterior distributions obtained by the UKI at the 15th iteration are depicted in Fig. 7. The UKI delivers a very similar posterior distribution, but at a significantly cheaper computational cost.

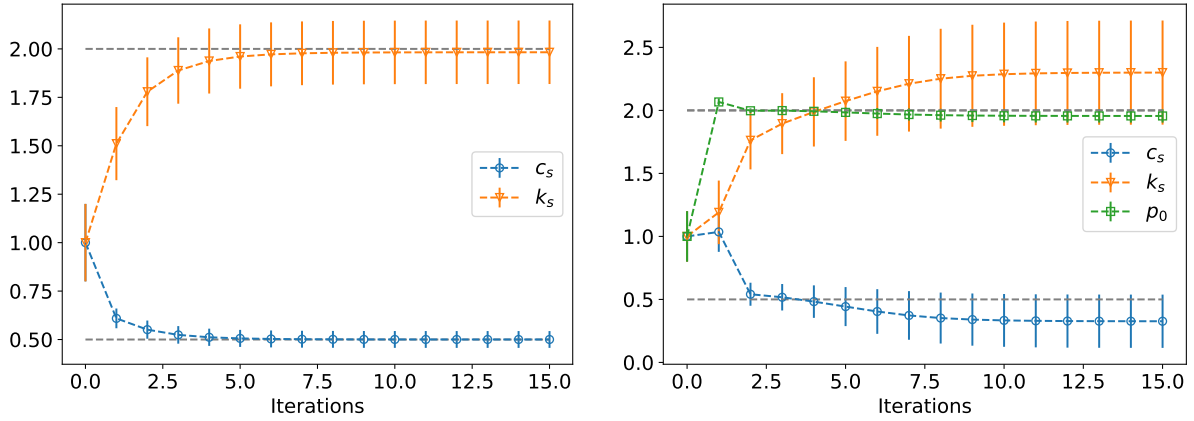


FIGURE 6 Convergence of the piston model problem with UKI for both 2-parameter (left) and 3-parameter (left) scenarios; the true parameter values are represented by dashed grey lines. The error bar associated with each data point denotes the $2 - \sigma$ confidence intervals.

4.2 | Airfoil Damage Detection Problem

The second test is a challenging real-world FSI problem associated with a damaged AGARD wing¹⁰⁴ undergoing transonic buffet. We consider a cruise condition, where the atmospheric density is $\rho_\infty = 0.61 \times 10^{-7}$ slug/in³ and the atmospheric pressure is $p_\infty = 6$ slugs/(in · s²); the free-stream Mach number is $M_\infty = 0.97$; and the angle of attack is $\alpha = 7.5^\circ$. The AGARD wing structure is modeled as a nonlinear elastic composite shell (See Fig. 8-left). The orthotropic properties of this material are density $\rho_s = 4.6 \times 10^{-4}$ slug/in³, parallel young's modulus $E_1 = 5.874 \times 10^6$ slug/(in · s²), orthogonal young's modulus $E_2 = 7.20 \times 10^6$ slug/(in · s²), rigidity modulus $G = 7.1688 \times 10^5$ slug/(in · s²), and Poisson's ratio $\nu = 0.31$. The physical dimensions are reported in Table 1. The thickness distribution is governed by the airfoil shape.

TABLE 1 Geometrical properties of the AGARD wing.

Parameter	Type/Value
Wingspan	30 inches
Root chord	21.96 inches
Tip chord	14.5 inches
Sweep	45°

The computational fluid domain $[-100'', 150''] \times [0'', 150''] \times [-100'', 100'']$ is discretized by the three-dimensional tetrahedral Eulerian mesh. The mesh contains 218,880 vertices and 1,248,912 tetrahedral elements, with a 0.75 inch resolution near the AGARD wing (See Fig. 8-right). The AGARD wing finite element model¹⁰⁵ consists of 800 triangular composite shell elements and 2,646 degrees of freedom (See Fig. 8-left-top). The embedded surface, representing the wing skin surface, consists of 2788 triangles (See Fig. 8-left-bottom).

The damage in airfoil is assumed to be isotropic elasticity-based damage in the spar direction (y -direction) with

$$E_1^d(y, \theta) = (1 - \omega(y, \theta)) E_1 \quad E_2^d(y, \theta) = (1 - \omega(y, \theta)) E_2 \quad \text{and} \quad G^d(y, \theta) = (1 - \omega(y, \theta)) G.$$

Here $\omega(y, \theta)$ is the scalar-valued damage variable, which varies between $\omega_{min} = -0.1$ (hardening) to $\omega_{max} = 0.9$ (softening):

$$\omega(y, \theta) = \frac{\omega_{max} - \omega_{min}}{1 - \frac{\omega_{max}}{\omega_{min}} \exp(\log a(y, \theta))} + \omega_{min}, \quad (24)$$

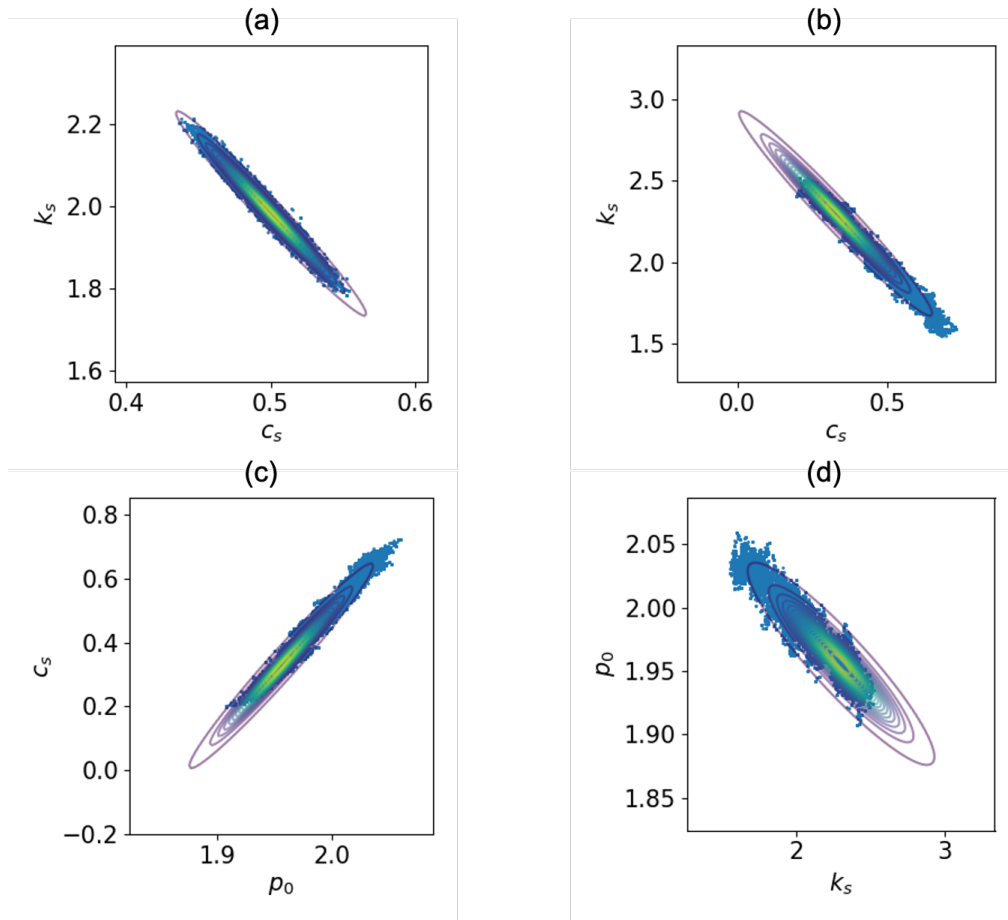


FIGURE 7 Pairwise posterior distribution of the piston model problem for both 2-parameter (a) and 3-parameter (b-d) scenarios. Contour plot: the posterior distribution obtained by the UKI at the 15th iteration; blue dots: reference posterior distribution obtained by MCMC.

where the random field $\log a(y, \theta)$, depending on parameters $\theta \in \mathbb{R}^{N_\theta}$, is modeled as a log-Gaussian field with covariance operator

$$\mathbf{C} = (-\Delta + \tau^2)^{-d}.$$

Here, $-\Delta$ denotes the Laplacian subject to homogeneous Neumann boundary conditions on the space of spatial-mean zero functions, $\tau = 2$ denotes the inverse length scale of the random field and $d = 1$ determines its regularity. The log-Gaussian field is approximated by the following Karhunen-Loève (KL) expansion

$$\log a(y, \theta) = \sum_{l=1}^{+\infty} \theta_{(l)} \sqrt{\lambda_l} \psi_l(y), \quad (25)$$

and the eigenpairs are of the form

$$\psi_l(y) = \sqrt{2} \cos(\pi l y) \quad \text{and} \quad \lambda_l = (\pi^2 l^2 + \tau^2)^{-d},$$

and $\theta_{(l)} \sim \mathcal{N}(0, 1)$ are independent and identically distributed. The mean state of $\log a(y, \theta) = 0$ corresponds to the undamaged state $\omega(y, \theta) = 0$.

For the forward problem, implicit backward Euler time integrator is used for the fluid and implicit 2nd order mid-point rule time integrator is applied to for the structure with a constant time step $\Delta t = 5 \times 10^{-5} s$. The simulation starts from a steady flow field depicted in Fig. 9, in which a shock wave forms on the airfoil. When the coupled simulation starts, the airfoil starts buffeting, interacts with the shock wave, and undergoes large deformations (See Fig. 10). The coupled system is integrated till $T = 0.1 s$. And each forward run takes about 36 core hours.

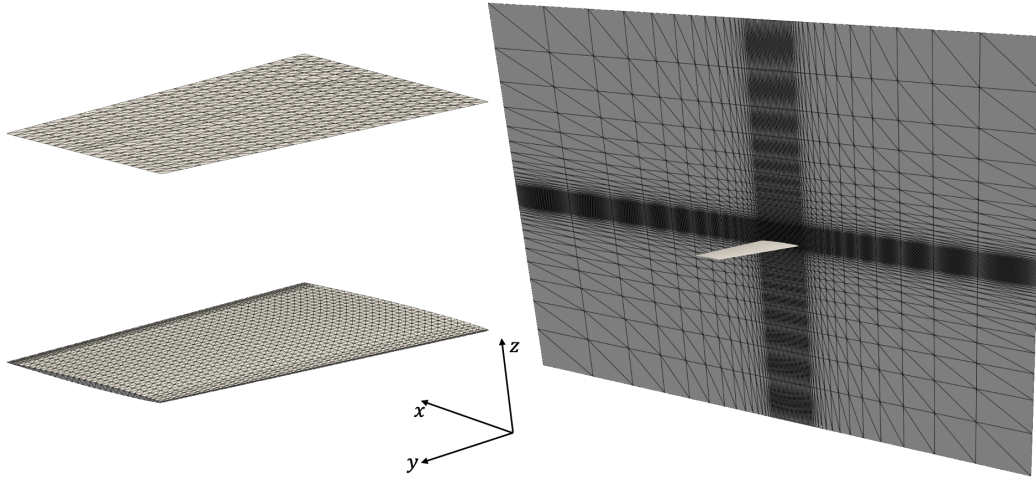


FIGURE 8 Computational models for the AGARD wing: finite element structural model (left-top), the wing skin surface of this model (left-bottom), and CFD mesh (right).

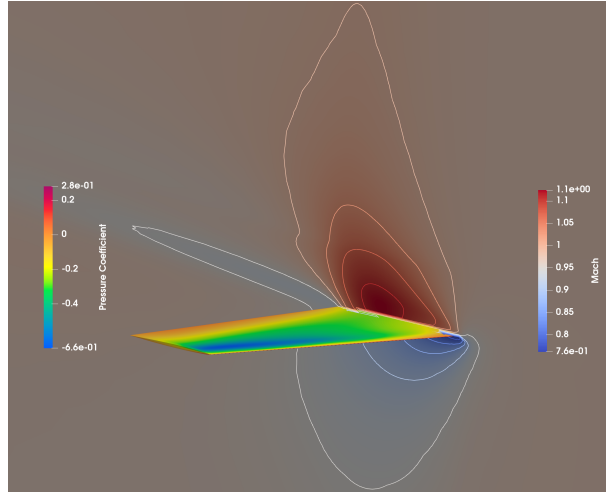


FIGURE 9 Initial condition for the FSI simulation: pressure coefficient on the wing and Mach contour profile in the fluid. The initial condition is also the converged steady state result with a fixed AGARD wing.

For the inverse problem, the damage field $\omega(y, \theta)$ is inferred from the displacement measurements of the airfoil buffeting motion. The reference damage field $\omega_{ref}(y)$ is generated from Eqs. (24) and (25) with the first 10 KL modes. The damage field $\omega_{ref}(y)$ is depicted in Fig. 11. With the reference damage field, we construct the observation y_{obs} at 12 locations (See Fig. 11) on the leading edge, half chord position, and trailing edge with 5% synthetic Gaussian random noises:

$$y_{obs} = y_{ref} + 5\%y_{ref} \odot \mathcal{N}(0, \mathbb{I}),$$

where \odot denotes element-wise multiplication. The observation data are collected every 0.002 s, giving $N_y = 600$ observation data in total (See Fig. 14).

The UKI is applied to retrieve the first $N_\theta = 5$ KL modes; in essence the model form error exists. The solution process is initialized with $m_0 = 0$ (no damage) and $C_0 = \mathbb{I}$, and hence $\theta_0 \sim \mathcal{N}(0, \mathbb{I})$. The observation error is set to follow $\eta \sim \mathcal{N}(0, 0.1^2\mathbb{I})$;

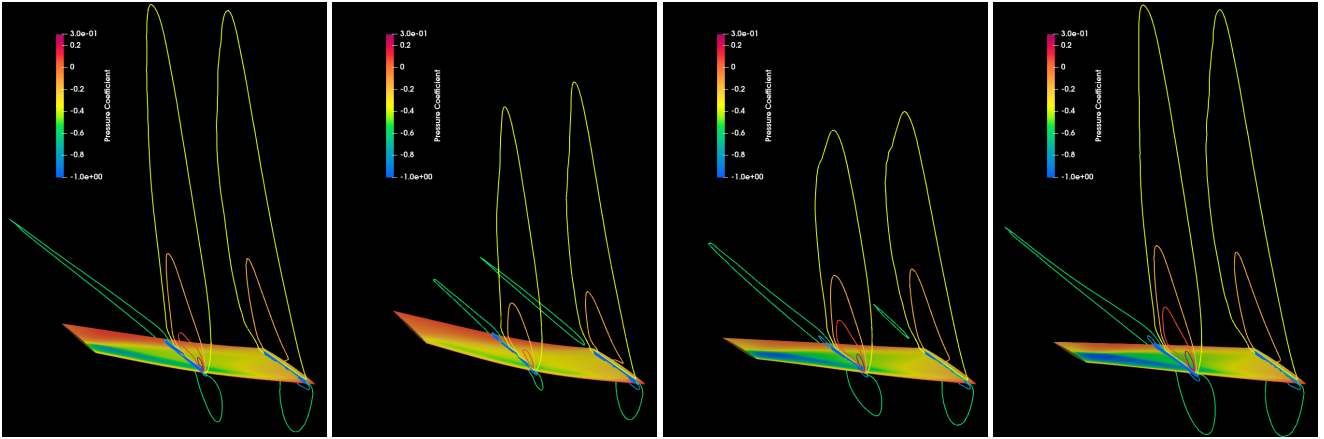


FIGURE 10 AGARD wing transonic buffet: Snapshots of the fluid-structure solution at $t = 0.025$ s, $t = 0.05$ s, $t = 0.075$ s, $t = 0.10$ s (left to right) with pressure coefficient on the wing and Mach contour in the fluid.

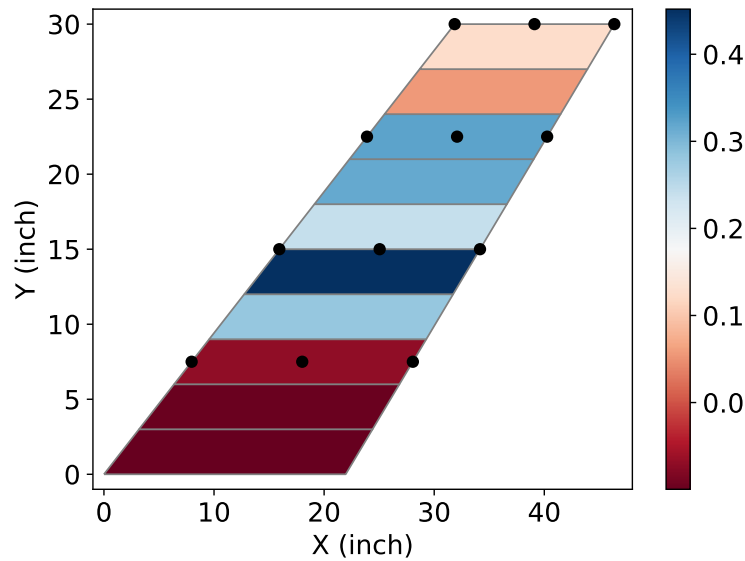


FIGURE 11 Reference damage field $\omega_{ref}(y)$ of the AGARD wing and the 12 pointwise measurement locations (black dots).

in essence we assume imperfect knowledge of the noise model. For $N_\theta = 5$, each iteration includes 11 parallel forward runs. The optimization errors $\Phi(\theta)$ in Eq. (3) at each iteration are plotted in Fig. 12, showing fast convergence. The estimated damage field $\omega(y, \theta)$ and the associated $2\text{-}\sigma$ confidence intervals at the 15-th iteration are depicted in Fig. 13. The truth damage field ω_{ref} falls within the confidence interval with high probability. The predicted displacement fields at these measurement locations and the displacement predicted with the initial guess (no-damage case) are depicted in Fig. 14. It is worth mentioning that all displacement curves are very close to the observation data, which indicates the wing displacement is not very sensitive to the damage. However, UKI still delivers a good estimate of the damage field, which demonstrates the effectiveness of the Bayesian calibration procedure for real-world applications.

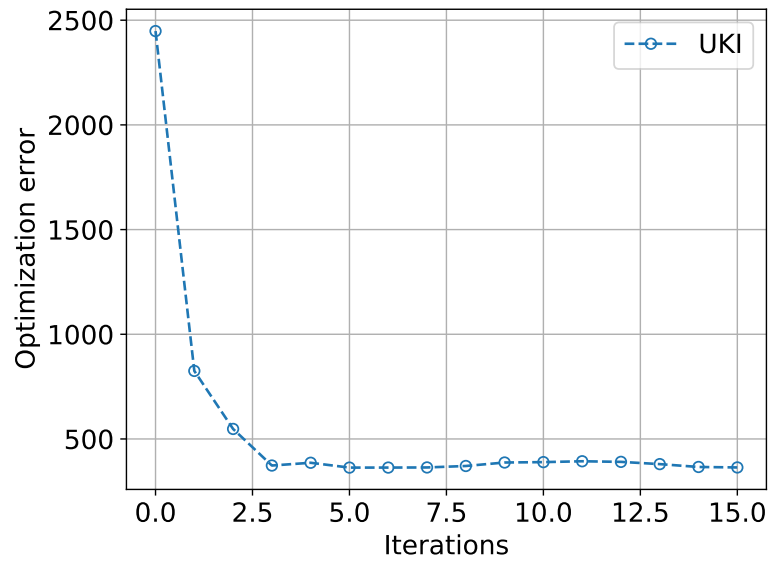


FIGURE 12 The optimization error $\frac{1}{2} \|\Sigma_\eta^{-\frac{1}{2}}(y - \mathcal{G}(\theta))\|^2$ at each UKI iteration for the airfoil damage detection problem.

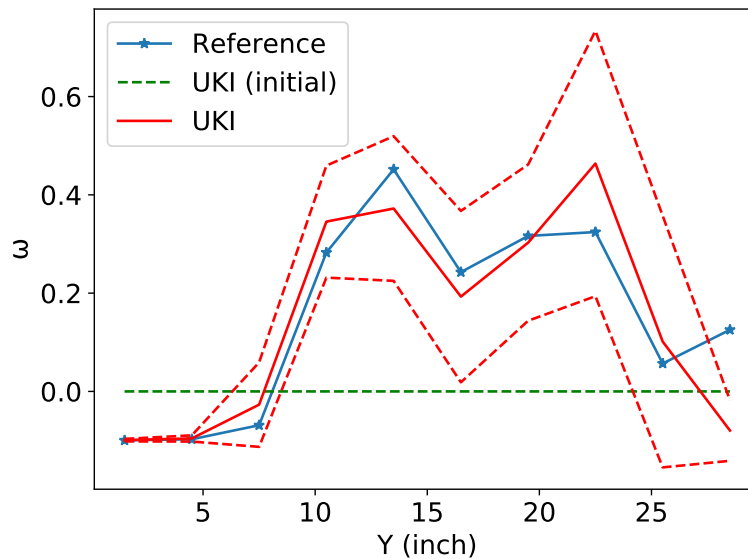


FIGURE 13 The estimated damage field $\omega(y, \theta_n)$ (red solid line) and the associated $2\text{-}\sigma$ confidence intervals (red dashed lines) at the 15-th iteration; The reference damage field $\omega_{ref}(y)$ (blue star line); The initial guess of the damage field at the 0-th iteration (green dashed line) for the airfoil damage detection problem.

5 | CONCLUSION

This paper presents a general Bayesian calibration framework for FSI problems based on unscented Kalman inversion. It is attractive for at least four reasons: i) It is non-intrusive and derivative-free; ii) It is robust for chaotic inverse problems with noisy observations; iii) It provides uncertainty information; iv) It is embarrassingly parallel. It is well-adapted to parameter/field estimation problems for any large complex computational models given as a black box. There are numerous directions for future improvements:

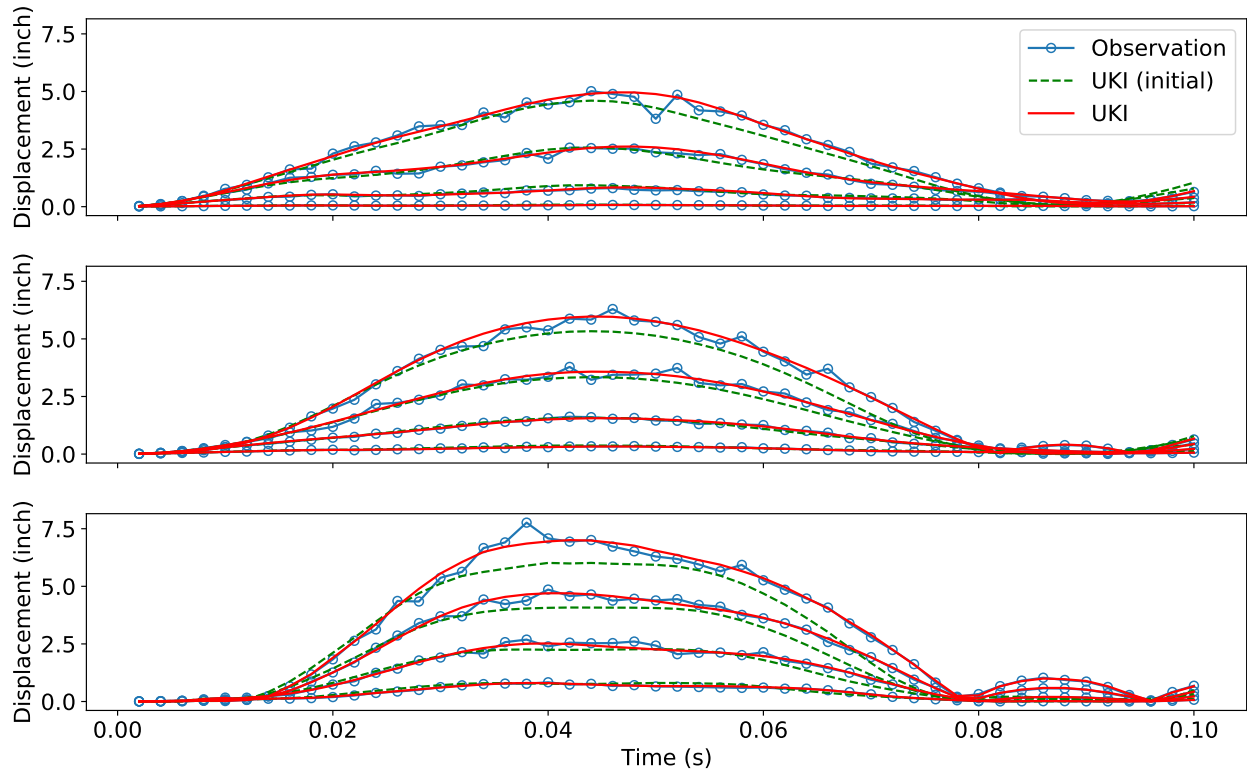


FIGURE 14 Blue dot lines: displacement observation data on the leading edge measurement locations (top), on the half-chord measurement locations (middle), on the trailing edge measurement locations (bottom) with the damaged AGARD wing. Dashed green lines: predictions with the initial guess (no damage). Red lines: predictions with the damage field obtained by the UKI at the 15th iteration.

- At each iteration, UKI requires solving the forward problem $2N_\theta + 1$ times. Although these forward solver evaluations are embarrassingly parallel, the computational cost might be intractable when the number of parameters N_θ is large or the forward evaluation is expensive. Low-resolution reduced-order model has been applied to accelerate the UKI iteration in the work of Huang *et al.*⁸⁵. The use of other reduced-order models, including but not limit to neural network surrogate models^{106,107,108,109,110}, projection-based reduced order models^{111,112,113,114,115}, and Kernel-based surrogate models^{116,117,118}, is worth exploring in the future.
- For the damage detection problem in Subsection 4.2, the sensors are uniformly located on the airfoil. Optimal sensor placement^{119,120,121}, which potentially makes data collection more efficient and makes the algorithm converge faster, is worth further investigation. And more realistic damage and fracture models^{122,123,124} will be considered in the future.
- For Bayesian calibration problems with time-series data studied in the present work, other Kalman methodology (e.g. Kalman smoother^{125,126,127}) will be applied and studied in the future.

6 | ACKNOWLEDGEMENT*

The authors gratefully acknowledge the support of National Institutes of Health under Award P01-DK043881 and the generosity of Eric and Wendy Schmidt by recommendation of the Schmidt Futures program. The authors thank Dr. Kevin G. Wang and Dr. Fangbao Tian for their advice on the manuscript.

References

1. Geuzaine P, Brown G, Harris C, Farhat C. Aeroelastic dynamic analysis of a full F-16 configuration for various flight conditions. *AIAA journal* 2003; 41(3): 363–371.
2. Kamakoti R, Shyy W. Fluid–structure interaction for aeroelastic applications. *Progress in Aerospace Sciences* 2004; 40(8): 535–558.
3. Dowell E. Some recent advances in nonlinear aeroelasticity: fluid-structure interaction in the 21st century. In: AIAA. ; 2010: 3137.
4. Huang Z, Avery P, Farhat C, Rabinovitch J, Derkevorkian A, Peterson LD. Simulation of parachute inflation dynamics using an Eulerian computational framework for fluid-structure interfaces evolving in high-speed turbulent flows. In: AIAA. ; 2018: 1540.
5. Huang DZ, Avery P, Farhat C, Rabinovitch J, Derkevorkian A, Peterson LD. Modeling, simulation and validation of supersonic parachute inflation dynamics during Mars landing. In: AIAA. ; 2020: 0313.
6. Avery P, Huang DZ, He W, Ehlers J, Derkevorkian A, Farhat C. A computationally tractable framework for nonlinear dynamic multiscale modeling of membrane woven fabrics. *International Journal for Numerical Methods in Engineering* 2021.
7. Hsu MC, Kamensky D, Bazilevs Y, Sacks MS, Hughes TJ. Fluid–structure interaction analysis of bioprosthetic heart valves: significance of arterial wall deformation. *Computational mechanics* 2014; 54(4): 1055–1071.
8. Updegrove A, Wilson NM, Merkow J, Lan H, Marsden AL, Shadden SC. SimVascular: an open source pipeline for cardiovascular simulation. *Annals of biomedical engineering* 2017; 45(3): 525–541.
9. Bertaglia G, Caleffi V, Pareschi L, Valiani A. Uncertainty quantification of viscoelastic parameters in arterial hemodynamics with the a-FSI blood flow model. *Journal of Computational Physics* 2021; 430: 110102.
10. Cao S, Zhang Y, Liao D, Zhong P, Wang KG. Shock-induced damage and dynamic fracture in cylindrical bodies submerged in liquid. *International journal of solids and structures* 2019; 169: 55–71.
11. Cao S, Wang G, Coutier-Delgosha O, Wang K. Shock-induced bubble collapse near solid materials: effect of acoustic impedance. *Journal of Fluid Mechanics* 2021; 907.
12. Ismail M, Wall WA, Gee MW. Adjoint-based inverse analysis of windkessel parameters for patient-specific vascular models. *Journal of Computational Physics* 2013; 244: 113–130.
13. Arthurs CJ, Xiao N, Moireau P, Schaeffter T, Figueroa CA. A flexible framework for sequential estimation of model parameters in computational hemodynamics. *Advanced modeling and simulation in engineering sciences* 2020; 7(1): 1–37.
14. Sohn H, Law KH. A Bayesian probabilistic approach for structure damage detection. *Earthquake engineering & structural dynamics* 1997; 26(12): 1259–1281.
15. Tuegel EJ, Ingraffea AR, Eason TG, Spottswood SM. Reengineering aircraft structural life prediction using a digital twin. *International Journal of Aerospace Engineering* 2011; 2011.
16. Sotoudehnia E, Shahabian F, Sani AA. A new method for damage detection of fluid-structure systems based on model updating strategy and incomplete modal data. *Ocean Engineering* 2019; 187: 106200.
17. Löhner R, Baum JD, Mestreau E, Sharov D, Charman C, Pelessone D. Adaptive embedded unstructured grid methods. *International Journal for Numerical Methods in Engineering* 2004; 60(3): 641–660.
18. Wang K, Rallu A, Gerbeau JF, Farhat C. Algorithms for interface treatment and load computation in embedded boundary methods for fluid and fluid–structure interaction problems. *International Journal for Numerical Methods in Fluids* 2011; 67(9): 1175–1206. doi: 10.1002/flid.2556

19. Farhat C, Gerbeau JF, Rallu A. FIVER: A finite volume method based on exact two-phase Riemann problems and sparse grids for multi-material flows with large density jumps. *Journal of Computational Physics* 2012; 231(19): 6360–6379. doi: <https://doi.org/10.1016/j.jcp.2012.05.026>
20. Lakshminarayan V, Farhat C, Main A. An embedded boundary framework for compressible turbulent flow and fluid–structure computations on structured and unstructured grids. *International Journal for Numerical Methods in Fluids* 2014; 76(6): 366–395. doi: [10.1002/flid.3937](https://doi.org/10.1002/flid.3937)
21. Main A, Zeng X, Avery P, Farhat C. An enhanced FIVER method for multi-material flow problems with second-order convergence rate. *Journal of Computational Physics* 2017; 329: 141–172. doi: <https://doi.org/10.1016/j.jcp.2016.10.028>
22. Peskin CS. Flow patterns around heart valves: A numerical method. *Journal of Computational Physics* 1972; 10(2): 252–271. doi: [https://doi.org/10.1016/0021-9991\(72\)90065-4](https://doi.org/10.1016/0021-9991(72)90065-4)
23. Fadlun E, Verzicco R, Orlandi P, Mohd-Yusof J. Combined immersed-boundary finite-difference methods for three-dimensional complex flow simulations. *Journal of Computational Physics* 2000; 161(1): 35–60. doi: <https://doi.org/10.1006/jcph.2000.6484>
24. Kim J, Kim D, Choi H. An immersed-boundary finite-volume method for simulations of flow in complex geometries. *Journal of Computational Physics* 2001; 171(1): 132–150. doi: <https://doi.org/10.1006/jcph.2001.6778>
25. Uhlmann M. An immersed boundary method with direct forcing for the simulation of particulate flows. *Journal of Computational Physics* 2005; 209(2): 448–476.
26. Choi JI, Oberoi RC, Edwards JR, Rosati JA. An immersed boundary method for complex incompressible flows. *Journal of Computational Physics* 2007; 224(2): 757–784. doi: <https://doi.org/10.1016/j.jcp.2006.10.032>
27. Taira K, Colonius T. The immersed boundary method: a projection approach. *Journal of Computational Physics* 2007; 225(2): 2118–2137.
28. Tian FB, Dai H, Luo H, Doyle JF, Rousseau B. Fluid–structure interaction involving large deformations: 3D simulations and applications to biological systems. *Journal of computational physics* 2014; 258: 451–469.
29. Ingram DM, Causon DM, Mingham CG. Developments in Cartesian cut cell methods. *Mathematics and Computers in Simulation* 2003; 61(3): 561–572. doi: [https://doi.org/10.1016/S0378-4754\(02\)00107-6](https://doi.org/10.1016/S0378-4754(02)00107-6)
30. Schott B, Ager C, Wall WA. Monolithic cut finite element–based approaches for fluid–structure interaction. *International Journal for Numerical Methods in Engineering* 2019.
31. Berger M, Aftosmis M. Progress towards a Cartesian cut-cell method for viscous compressible flow. In: AIAA. ; 2012: 1301.
32. Johansen H, Colella P. A Cartesian grid embedded boundary method for Poisson’s equation on irregular domains. *Journal of Computational Physics* 1998; 147(1): 60–85. doi: <https://doi.org/10.1006/jcph.1998.5965>
33. Uddin H, Kramer R, Pantano C. A Cartesian-based embedded geometry technique with adaptive high-order finite differences for compressible flow around complex geometries. *Journal of Computational Physics* 2014; 262: 379–407. doi: [10.1016/j.jcp.2014.01.004](https://doi.org/10.1016/j.jcp.2014.01.004)
34. Harris RE. Adaptive Cartesian immersed boundary method for simulation of flow over flexible geometries. *AIAA Journal* 2012; 51(1): 53–69. doi: [10.1006/jcph.1999.6293](https://doi.org/10.1006/jcph.1999.6293)
35. Almgren AS, Bell JB, Colella P, Marthaler T. A Cartesian grid projection method for the incompressible Euler equations in complex geometries. *SIAM Journal on Scientific Computing* 1997; 18(5): 1289–1309. doi: [10.1137/S1064827594273730](https://doi.org/10.1137/S1064827594273730)
36. Balaras E. Modeling complex boundaries using an external force field on fixed Cartesian grids in large-eddy simulations. *Computers & Fluids* 2004; 33(3): 375–404. doi: [https://doi.org/10.1016/S0045-7930\(03\)00058-6](https://doi.org/10.1016/S0045-7930(03)00058-6)

37. Tseng YH, Ferziger JH. A ghost-cell immersed boundary method for flow in complex geometry. *Journal of computational physics* 2003; 192(2): 593–623. doi: <https://doi.org/10.1016/j.jcp.2003.07.024>
38. Feng ZG, Michaelides EE. The immersed boundary-lattice Boltzmann method for solving fluid–particles interaction problems. *Journal of computational physics* 2004; 195(2): 602–628.
39. Tian FB, Luo H, Zhu L, Liao JC, Lu XY. An efficient immersed boundary-lattice Boltzmann method for the hydrodynamic interaction of elastic filaments. *Journal of computational physics* 2011; 230(19): 7266–7283.
40. Yang X, Zhang X, Li Z, He GW. A smoothing technique for discrete delta functions with application to immersed boundary method in moving boundary simulations. *Journal of Computational Physics* 2009; 228(20): 7821–7836.
41. Goza A, Liska S, Morley B, Colonius T. Accurate computation of surface stresses and forces with immersed boundary methods. *Journal of Computational Physics* 2016; 321: 860–873.
42. Ho J, Farhat C. Discrete embedded boundary method with smooth dependence on the evolution of a fluid-structure interface. *International Journal for Numerical Methods in Engineering* 2020.
43. Ho JB, Farhat C. Aerodynamic Shape Optimization using an Embedded Boundary Method with Smoothness Guarantees. In: AIAA. ; 2021: 0280.
44. Berger MJ, Colella P, others . Local adaptive mesh refinement for shock hydrodynamics. *Journal of computational Physics* 1989; 82(1): 64–84.
45. Griffith BE, Hornung RD, McQueen DM, Peskin CS. An adaptive, formally second order accurate version of the immersed boundary method. *Journal of computational physics* 2007; 223(1): 10–49.
46. Borker R, Huang D, Grimberg S, Farhat C, Avery P, Rabinovitch J. Mesh adaptation framework for embedded boundary methods for computational fluid dynamics and fluid-structure interaction. *International Journal for Numerical Methods in Fluids* 2019; 90(8): 389–424.
47. Hirt CW, Amsden AA, Cook J. An arbitrary Lagrangian-Eulerian computing method for all flow speeds. *Journal of computational physics* 1974; 14(3): 227–253.
48. Tezduyar TE, Behr M, Mittal S, Liou J. A new strategy for finite element computations involving moving boundaries and interfaces—the deforming-spatial-domain/space-time procedure: II. Computation of free-surface flows, two-liquid flows, and flows with drifting cylinders. *Computer methods in applied mechanics and engineering* 1992; 94(3): 353–371.
49. Felippa CA, Park KC, Farhat C. Partitioned analysis of coupled mechanical systems. *Computer methods in applied mechanics and engineering* 2001; 190(24-25): 3247–3270.
50. Küttler U, Wall WA. Fixed-point fluid–structure interaction solvers with dynamic relaxation. *Computational mechanics* 2008; 43(1): 61–72.
51. Huang DZ, Persson PO, Zahr MJ. High-order, linearly stable, partitioned solvers for general multiphysics problems based on implicit–explicit Runge–Kutta schemes. *Computer Methods in Applied Mechanics and Engineering* 2019; 346: 674–706.
52. Huang DZ, Pazner W, Persson PO, Zahr MJ. High-order partitioned spectral deferred correction solvers for multiphysics problems. *Journal of Computational Physics* 2020: 109441.
53. Huang DZ, Zahr MJ, Persson PO. A high-order partitioned solver for general multiphysics problems and its applications in optimization. In: AIAA. ; 2019: 1697.
54. Dukowicz JK, Kodis JW. Accurate conservative remapping (rezoning) for arbitrary Lagrangian-Eulerian computations. *SIAM Journal on Scientific and Statistical Computing* 1987; 8(3): 305–321.
55. Long C, Marsden A, Bazilevs Y. Fluid–structure interaction simulation of pulsatile ventricular assist devices. *Computational Mechanics* 2013; 52(5): 971–981.

56. Kaipio J, Somersalo E. *Statistical and computational inverse problems*. 160. Springer Science & Business Media . 2006.
57. Dashti M, Stuart AM. The Bayesian approach to inverse problems. *arXiv preprint arXiv:1302.6989* 2013.
58. Geyer CJ. Practical markov chain monte carlo. *Statistical science* 1992; 473–483.
59. Gelman A, Gilks WR, Roberts GO. Weak convergence and optimal scaling of random walk Metropolis algorithms. *The annals of applied probability* 1997; 7(1): 110–120.
60. Goodman J, Weare J. Ensemble samplers with affine invariance. *Communications in applied mathematics and computational science* 2010; 5(1): 65–80.
61. Kalman RE. A new approach to linear filtering and prediction problems. *J. Basic Eng. Mar* 1960; 82(1): 35–45.
62. Sorenson HW. *Kalman filtering: theory and application*. IEEE . 1985.
63. Evensen G. Sequential data assimilation with a nonlinear quasi-geostrophic model using Monte Carlo methods to forecast error statistics. *Journal of Geophysical Research: Oceans* 1994; 99(C5): 10143–10162.
64. Julier SJ, Uhlmann JK, Durrant-Whyte HF. A new approach for filtering nonlinear systems. In: . 3. IEEE. ; 1995: 1628–1632.
65. Wan EA, Van Der Merwe R. The unscented Kalman filter for nonlinear estimation. In: Ieee. ; 2000: 153–158.
66. Arasaratnam I, Haykin S. Cubature kalman filters. *IEEE Transactions on automatic control* 2009; 54(6): 1254–1269.
67. Anderson JL. An ensemble adjustment Kalman filter for data assimilation. *Monthly weather review* 2001; 129(12): 2884–2903.
68. Bishop CH, Etherton BJ, Majumdar SJ. Adaptive sampling with the ensemble transform Kalman filter. Part I: Theoretical aspects. *Monthly weather review* 2001; 129(3): 420–436.
69. Wan EA, Nelson AT. Neural dual extended Kalman filtering: applications in speech enhancement and monaural blind signal separation. In: IEEE. ; 1997: 466–475.
70. Gu Y, Oliver DS. The ensemble Kalman filter for continuous updating of reservoir simulation models. 2006.
71. Oliver DS, Reynolds AC, Liu N. *Inverse theory for petroleum reservoir characterization and history matching*. Cambridge University Press . 2008.
72. Chen Y, Oliver DS. Ensemble randomized maximum likelihood method as an iterative ensemble smoother. *Mathematical Geosciences* 2012; 44(1): 1–26.
73. Iglesias MA, Law KJ, Stuart AM. Ensemble Kalman methods for inverse problems. *Inverse Problems* 2013; 29(4): 045001.
74. Huang DZ, Schneider T, Stuart AM. Unscented kalman inversion. *arXiv preprint arXiv:2102.01580* 2021.
75. Iglesias MA. A regularizing iterative ensemble Kalman method for PDE-constrained inverse problems. *Inverse Problems* 2016; 32(2): 025002.
76. Schillings C, Stuart AM. Analysis of the ensemble Kalman filter for inverse problems. *SIAM Journal on Numerical Analysis* 2017; 55(3): 1264–1290.
77. Schneider T, Lan S, Stuart A, Teixeira J. Earth system modeling 2.0: A blueprint for models that learn from observations and targeted high-resolution simulations. *Geophysical Research Letters* 2017; 44(24): 12–396.
78. Schillings C, Stuart AM. Convergence analysis of ensemble Kalman inversion: the linear, noisy case. *Applicable Analysis* 2018; 97(1): 107–123.
79. Iglesias M, Yang Y. Adaptive regularisation for ensemble Kalman inversion with applications to non-destructive testing and imaging. *arXiv preprint arXiv:2006.14980* 2020.

80. Chada NK, Chen Y, Sanz-Alonso D. Iterative Ensemble Kalman Methods: A Unified Perspective with Some New Variants. *arXiv preprint arXiv:2010.13299* 2020.
81. Gao H, Wang JX. A Bi-fidelity ensemble kalman method for PDE-constrained inverse problems in computational mechanics. *Computational Mechanics* 2021; 67(4): 1115–1131.
82. Zhang XL, Xiao H, He GW, Wang SZ. Assimilation of disparate data for enhanced reconstruction of turbulent mean flows. *Computers & Fluids* 2021: 104962.
83. Julier SJ, Uhlmann JK. New extension of the Kalman filter to nonlinear systems. In: . 3068. International Society for Optics and Photonics. ; 1997: 182–193.
84. Huang DZ, Huang J. Unscented Kalman Inversion: Efficient Gaussian Approximation to the Posterior Distribution. *arXiv preprint arXiv:2103.00277* 2021.
85. Huang DZ, Huang J. Improve Unscented Kalman Inversion With Low-Rank Approximation and Reduced-Order Model. *arXiv preprint arXiv:2102.10677* 2020.
86. Le Cam L, Yang GL. *Asymptotics in statistics: some basic concepts*. Springer Science & Business Media . 2012.
87. Vaart V. dAW. *Asymptotic statistics*. 3. Cambridge university press . 2000.
88. Freedman D, others . Wald Lecture: On the Bernstein-von Mises theorem with infinite-dimensional parameters. *Annals of Statistics* 1999; 27(4): 1119–1141.
89. Lu Y, Stuart A, Weber H. Gaussian Approximations for Probability Measures on \mathbb{R}^d . *SIAM/ASA Journal on Uncertainty Quantification* 2017; 5(1): 1136–1165.
90. Reich S, Cotter C. *Probabilistic forecasting and Bayesian data assimilation*. Cambridge University Press . 2015.
91. Law K, Stuart A, Zygalakis K. *Data assimilation*. Cham, Switzerland: Springer 2015.
92. Julier S, Uhlmann J, Durrant-Whyte HF. A new method for the nonlinear transformation of means and covariances in filters and estimators. *IEEE Transactions on automatic control* 2000; 45(3): 477–482.
93. Mogensen PK, Riseth AN. Optim: A mathematical optimization package for Julia. *Journal of Open Source Software* 2018; 3(24): 615. doi: 10.21105/joss.00615
94. Hager WW, Zhang H. Algorithm 851: CG_DESCENT, a conjugate gradient method with guaranteed descent. *ACM Transactions on Mathematical Software (TOMS)* 2006; 32(1): 113–137.
95. Farhat C, Rallu A, Wang K, Belytschko T. Robust and provably second-order explicit–explicit and implicit–explicit staggered time-integrators for highly non-linear compressible fluid–structure interaction problems. *International Journal for Numerical Methods in Engineering* 2010; 84(1): 73–107. doi: 10.1002/nme.2883
96. Wang K, Grétarsson J, Main A, Farhat C. Computational algorithms for tracking dynamic fluid–structure interfaces in embedded boundary methods. *International Journal for Numerical Methods in Fluids* 2012; 70(4): 515–535. doi: 10.1002/flid.3659
97. Huang DZ, De Santis D, Farhat C. A family of position-and orientation-independent embedded boundary methods for viscous flow and fluid–structure interaction problems. *Journal of Computational Physics* 2018; 365: 74–104.
98. Farhat C, Wang K, Main A, et al. Dynamic implosion of underwater cylindrical shells: experiments and computations. *International Journal of Solids and Structures* 2013; 50(19): 2943–2961. doi: <https://doi.org/10.1016/j.ijsolstr.2013.05.006>
99. Huang DZ, Avery P, Farhat C. An embedded boundary approach for resolving the contribution of cable subsystems to fully coupled fluid-structure interaction. *International Journal for Numerical Methods in Engineering* 2020.
100. Huang DZ, Wong ML, Lele SK, Farhat C. Homogenized Flux-Body Force Treatment of Compressible Viscous Porous Wall Boundary Conditions. *AIAA Journal* 2021: 1–15.

101. Roe PL. Approximate Riemann solvers, parameter vectors, and difference schemes. *Journal of computational physics* 1981; 43(2): 357–372.
102. Van Leer B. Towards the ultimate conservative difference scheme. V. A second-order sequel to Godunov's method. *Journal of computational Physics* 1979; 32(1): 101–136.
103. Main GA. *Implicit and Higher-order Discretization Methods for Compressible Multi-phase Fluid and Fluid-structure Problems*. PhD thesis. Stanford University, Stanford University; 2014.
104. Yates Jr EC. AGARD standard aeroelastic configurations for dynamic response. Candidate configuration I.-wing 445.6. 1987.
105. Lesoinne M, Sarkis M, Hetmaniuk U, Farhat C. A linearized method for the frequency analysis of three-dimensional fluid/structure interaction problems in all flow regimes. *Computer Methods in Applied Mechanics and Engineering* 2001; 190(24-25): 3121–3146.
106. Raissi M, Perdikaris P, Karniadakis GE. Physics-informed neural networks: A deep learning framework for solving forward and inverse problems involving nonlinear partial differential equations. *Journal of Computational Physics* 2019; 378: 686–707.
107. Huang DZ, Xu K, Farhat C, Darve E. Learning constitutive relations from indirect observations using deep neural networks. *Journal of Computational Physics* 2020; 109491.
108. Xu K, Huang DZ, Darve E. Learning constitutive relations using symmetric positive definite neural networks. *Journal of Computational Physics* 2021; 428: 110072.
109. Jimenez-Martinez M, Alfaro-Ponce M. Fatigue damage effect approach by artificial neural network. *International Journal of Fatigue* 2019; 124: 42–47.
110. Kovachki N, Liu B, Sun X, et al. Multiscale modeling of materials: Computing, data science, uncertainty and goal-oriented optimization. *arXiv preprint arXiv:2104.05918* 2021.
111. Dowell EH, Hall KC. Modeling of fluid-structure interaction. *Annual review of fluid mechanics* 2001; 33(1): 445–490.
112. Lieu T, Farhat C, Lesoinne M. Reduced-order fluid/structure modeling of a complete aircraft configuration. *Computer methods in applied mechanics and engineering* 2006; 195(41-43): 5730–5742.
113. Balajewicz M, Farhat C. Reduction of nonlinear embedded boundary models for problems with evolving interfaces. *Journal of Computational Physics* 2014; 274: 489–504.
114. Xiao D, Yang P, Fang F, Xiang J, Pain CC, Navon IM. Non-intrusive reduced order modelling of fluid–structure interactions. *Computer Methods in Applied Mechanics and Engineering* 2016; 303: 35–54.
115. Taira K, Brunton SL, Dawson ST, et al. Modal analysis of fluid flows: An overview. *Aiaa Journal* 2017; 55(12): 4013–4041.
116. Quinonero-Candela J, Rasmussen CE. A unifying view of sparse approximate Gaussian process regression. *The Journal of Machine Learning Research* 2005; 6: 1939–1959.
117. Hofmann T, Schölkopf B, Smola AJ. Kernel methods in machine learning. *The annals of statistics* 2008: 1171–1220.
118. Hamzi B, Maulik R, Owhadi H. Data-driven geophysical forecasting: Simple, low-cost, and accurate baselines with kernel methods. *arXiv preprint arXiv:2103.10935* 2021.
119. Worden K, Burrows A. Optimal sensor placement for fault detection. *Engineering structures* 2001; 23(8): 885–901.
120. Meo M, Zumpano G. On the optimal sensor placement techniques for a bridge structure. *Engineering structures* 2005; 27(10): 1488–1497.
121. Manohar K, Brunton BW, Kutz JN, Brunton SL. Data-driven sparse sensor placement for reconstruction: Demonstrating the benefits of exploiting known patterns. *IEEE Control Systems Magazine* 2018; 38(3): 63–86.

122. Moës N, Dolbow J, Belytschko T. A finite element method for crack growth without remeshing. *International journal for numerical methods in engineering* 1999; 46(1): 131–150.
123. Zhan Q, Sun Q, Ren Q, Fang Y, Wang H, Liu QH. A discontinuous Galerkin method for simulating the effects of arbitrary discrete fractures on elastic wave propagation. *Geophysical Journal International* 2017; 210(2): 1219–1230.
124. Zhan Q, Sun Q, Zhuang M, et al. A new upwind flux for a jump boundary condition applied to 3D viscous fracture modeling. *Computer Methods in Applied Mechanics and Engineering* 2018; 331: 456–473.
125. Evensen G, Van Leeuwen PJ. An ensemble Kalman smoother for nonlinear dynamics. *Monthly Weather Review* 2000; 128(6): 1852–1867.
126. Bocquet M, Sakov P. An iterative ensemble Kalman smoother. *Quarterly Journal of the Royal Meteorological Society* 2014; 140(682): 1521–1535.
127. Spratt JS, Rodriguez M, Schmidmayer K, et al. Characterizing viscoelastic materials via ensemble-based data assimilation of bubble collapse observations. *Journal of the Mechanics and Physics of Solids* 2021; 152: 104455.

